Spin crossover in ferropericlase and velocity heterogeneities in the lower mantle

Zhongqing Wu[a,1] and Renata M. Wentzcovitch[b,c,1]

[a]Laboratory of Seismology and Physics of Earth's Interior, School of Earth and Space Sciences, University of Science and Technology of China, Hefei 230026, People's Republic of China; and [b]Department of Chemical Engineering and Materials Science and [c]Minnesota Supercomputing Institute, University of Minnesota, Minneapolis, MN 55455

Edited* by Ho-kwang Mao, Carnegie Institution of Washington, Washington, DC, and approved May 30, 2014 (received for review December 3, 2013)

Deciphering the origin of seismic velocity heterogeneities in the mantle is crucial to understanding internal structures and processes at work in the Earth. The spin crossover in iron in ferropericlase (Fp), the second most abundant phase in the lower mantle, introduces unfamiliar effects on seismic velocities. First-principles calculations indicate that anticorrelation between shear velocity (V_S) and bulk sound velocity (V_φ) in the mantle, usually interpreted as compositional heterogeneity, can also be produced in homogeneous aggregates containing Fp. The spin crossover also suppresses thermally induced heterogeneity in longitudinal velocity (V_P) at certain depths but not in V_S. This effect is observed in tomography models at conditions where the spin crossover in Fp is expected in the lower mantle. In addition, the one-of-a-kind signature of this spin crossover in the $R_{S/P}$ ($\partial \ln V_S/\partial \ln V_P$) heterogeneity ratio might be a useful fingerprint to detect the presence of Fp in the lower mantle.

seismic tomography | lateral heterogeneity | elastic modulus | density functional theory | mantle plume

Ferropericlase (Fp) is believed to be the second most abundant phase in the lower mantle (1, 2). Since the discovery of the high-spin (HS) to low-spin (LS) crossover in iron in Fp (3), this phenomenon has been investigated extensively experimentally and theoretically (4–14). Most of its properties are affected by the spin crossover. In particular, thermodynamics (14) and thermal elastic properties (15–20) are modified in unusual ways that can change profoundly our understanding of the Earth's mantle. However, this is a broad and smooth crossover that takes place throughout most of the lower mantle and might not produce obvious signatures in radial velocity or density profiles (20, 21) (see Figs. S1 and S2). Therefore, its effects on aggregates are more elusive and indirect. For instance, the associated density anomaly can invigorate convection, as demonstrated by geodynamics simulations in a homogeneous mantle (22–24). The bulk modulus anomaly may decrease creep activation parameters and lower mantle viscosity (10, 24, 25) promoting mantle homogenization in the spin crossover region (24), and anomalies in elastic coefficients can enhance anisotropy in the lower mantle (16). Less understood are its effects on seismic velocities produced by lateral temperature variations.

The present analysis is based on our understanding of thermal elastic anomalies caused by the spin crossover. It has been challenging for both experiments (15–19) and theory (20) to reach a consensus on this topic. Measurements often seemed to include extrinsic effects, making it difficult to confirm the spin crossover signature by different techniques and across laboratories. A theoretical framework had to be developed to address these effects. However, an agreeable interpretation of data and results has emerged recently (20). With increasing pressure, nontrivial behavior is observed in all elastic coefficients, aggregate moduli, and density throughout the spin crossover—the mixed spin (MS) state. In an ideal crystal or aggregate, bulk modulus (K_S), C_{11}, and C_{12} are considerably reduced in the MS state, whereas shear modulus (G), C_{44}, and density (ρ) are enhanced. The pressure range of these anomalies broadens with increasing temperature whereas the magnitude decreases. With respect to the HS state, all these properties are enhanced in the LS state.

Results and Discussion

The nature of lateral (isobaric) heterogeneity produced by temperature variations in an Fp-bearing aggregate is better grasped by inspecting the temperature dependence of Fp's aggregate moduli and density. Along an adiabatic geotherm (26), spin crossovers manifest most strongly near 75 GPa (~1,750-km depth) in a pyrolitic mantle (Fig. S2). At this pressure, the bulk modulus softening anomaly in Fp, ΔK_S^{MS}, is maximum at ~1,400 K (Fig. 1). At these conditions $\Delta K_S^{MS} \sim -120$ GPa compared with $\Delta K_S^{HS\rightarrow LS} \sim 13$ GPa for $Mg_{0.875}Fe_{0.125}O$ (Fig. 1*A*). Below ~1,400 K, dK_S^{MS}/dT can be enhanced more than 20 times at ~920 K (Table 1). Above ~1,400 K, dK_S^{MS}/dT is positive and is 6 to 10 times larger than $\left|dK_S^{HS}/dT\right|$ at 1,850 K. This effect can be misinterpreted as compositional heterogeneity in the mantle. At ~1,400 K, $dK_S^{MS}/dT \sim 0$ GPa/K; that is, temperature anomalies do not manifest in the bulk modulus. In contrast, the shear modulus is most sensitive to temperature variations at ~1,400 K, and dG^{MS}/dT is enhanced more than two times. Density behaves similarly to G^{MS} (Table 1). In a pyrolitic aggregate, such anomalies are largely reduced (Fig. 1*B*), but the anticorrelation between dK_S^{MS}/dT and dG^{MS}/dT above ~1,400 K remains

Significance

Seismic tomography reveals Earth's internal structure in great detail. Lateral variations of seismic wave velocities expose enigmatic mantle structures that, to be deciphered, require independent knowledge of acoustic velocities in minerals. Using density functional theory-based computational methods we show that a spin state change in iron in ferropericlase, the second major phase of the Earth's lower mantle, produces seismic velocity anomalies that can be misinterpreted as compositional heterogeneity. This spin change reduces thermally induced longitudinal velocity variations between ~1,500- and 2,000-km depths. This phenomenon is observed in *P* velocity tomography models and has been thought to be related to a chemical transition in the mantle. The spin change in iron in ferropericlase may offer an alternative interpretation of this phenomenon.

Author contributions: Z.W. and R.M.W. designed research, performed research, analyzed data, and wrote the paper.

The authors declare no conflict of interest.

*This Direct Submission article had a prearranged editor.

Freely available online through the PNAS open access option.

[1]To whom correspondence may be addressed. Email: wuzq10@ustc.edu.cn or wentz002@umn.edu.

This article contains supporting information online at www.pnas.org/lookup/suppl/doi:10.1073/pnas.1322427111/-/DCSupplemental.

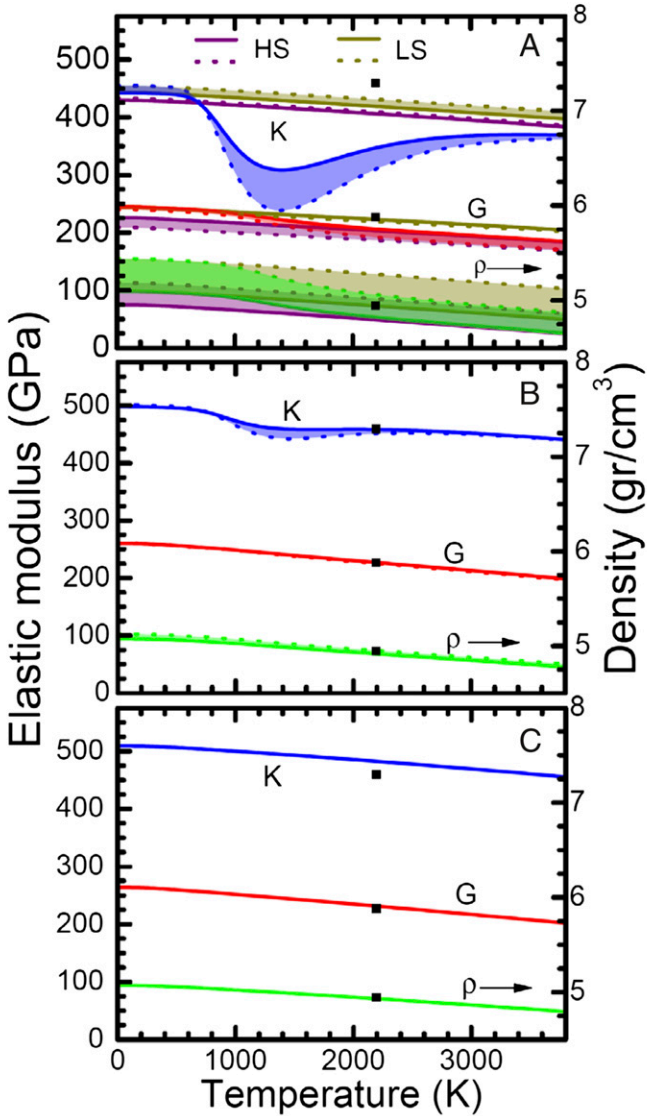

Fig. 1. Temperature dependence of bulk modulus, K_S; shear modulus, G; and density, ρ, at 75 GPa for (*A*) aggregates of Fp, $Mg_{0.875}Fe_{0.125}O$ (solid line) and $Mg_{0.79}Fe_{0.21}O$ (dotted line); (*B*) pyrolitic aggregates containing 78 wt % of $(Mg_{0.91}Fe_{0.09})SiO_3$ (MgPv), 7% $CaSiO_3$, 15 wt % $Mg_{0.875}Fe_{0.125}O$ (solid line), and same but $Mg_{0.79}Fe_{0.21}O$ (dotted line); and (*C*) a perovskitic aggregate containing 92 wt % $(Mg_{0.91}Fe_{0.09})SiO_3$ and 8 wt % $CaSiO_3$-Pv. Corresponding Preliminary Reference Earth Model values (65) at 75 GPa are shown as solid squares.

a striking feature. (See Fig. S3 for illustration of this effect at other temperatures.)

The potential influence of the spin crossover on seismic tomography is better understood by inspecting simultaneously its effects on all velocities and correlations among these effects at likely mantle conditions and compositions. Two geotherms are considered: an adiabatic one consistent with whole-mantle convection (26) and a superadiabatic one (27) more consistent with a chemically stratified mantle and layered convection. The analysis is carried out for compositionally homogeneous mantle models, and the aim is to expose trends. For contrast, the following uniform aggregates are considered: pure Fp, where effects are fully expressed, and pyrolitic and perovskitic aggregates. Elastic properties of iron-bearing perovskite (MgPv) and of $CaSiO_3$ perovskite (CaPv) used in these calculations are described in *Supporting Information*. The effect of a possible but unlikely spin crossover in ferric iron in MgPv (28–31) in the lower mantle is not considered here owing to its complexity, uncertainties, and unresolved issues. However, its potential effect is addressed later. Uniform mantles with several compositions are then examined between ~700 and ~2,600 km (25–120 GPa). Effects of the postperovskite phase change (32–34) should be avoided in this depth range.

Although crossover related anomalies in radial velocity profiles in a pyrolitic lower mantle might be subtle and hard to notice (Fig. S2), related lateral heterogeneities in bulk, $V_\varphi(R_{\varphi/T})$, and longitudinal velocities, $V_P(R_{P/T})$, are quite robust (Fig. 2). Uncertainties related to the geotherm do not preclude their expression as long as Fp is present in nonnegligible amounts in the mantle. Anomalies start manifesting at ~1,000-km depth (~38 GPa) and develop dramatically beyond 1,250 km (Fig. 2 *A* and *B*). Between ~1,500-km and 2,000-km depth, V_φ^{pyr} increases with increasing temperature; that is, $R_{\varphi/T}^{pyr}$ is positive (Fig. 2*A*). In contrast, beyond ~2,050 km (~90 GPa), $R_{\varphi/T}^{pyr}$ is negative, reaching a minimum somewhere between ~2,350- and 2,620-km depth. The related anomaly in V_S, $R_{S/T}^{pyr}$, is barely discernible; that is, V_S^{pyr} is basically insensitive to the spin crossover (Fig. 2*C*). Consequently, the anomaly in V_P, $R_{P/T}^{pyr}$, although similar, is more subtle than that in $R_{\varphi/T}^{pyr}$ (Fig. 2*B*). Depending on Fp abundance and composition, $R_{P/T}^{pyr}$ can be positive, vanish, or remain negative as in a perovskitic mantle (Fig. 2*B*). As long as Fp is present in detectable amounts, the magnitude of $R_{P/T}^{pyr}$ should be reduced in the mid–lower mantle (Fig. 2*B* and caption). This result translated into velocity heterogeneity in a pyrolitic mantle (see results for pyr in Fig. 2*B* caption) implies that a lateral temperature change of $\Delta T_l \sim \pm\ 500$ K manifests at ~1,100-km depth or between ~2,350- and 2,620-km depths as $\Delta V_P \sim 1\%$, whereas between 1,650 and 1,800 km it produces $\Delta V_P \sim 0.3\%$. For a pyrolitic mantle with 18 wt % of $Mg_{0.81}Fe_{0.19}O$, $\Delta V_P \sim 0\%$ at 73 GPa (~1,720 km) along the adiabatic geotherm (26). Along the superadiabatic geotherm (27), $\Delta V_P \sim 0\%$ at 78 GPa (~1,820 km) for a mantle with 21 wt % of $Mg_{0.81}Fe_{0.19}O$. These are typical pyrolitic compositions (1, 3, 35).

This suppression of lateral variations in V_P at ~1,700 km correlates with a similar and well-known global feature (36) believed to correspond to a compositional transition (37) to a denser (~4%) layer in the deep lower mantle (38). For comparison, the spin crossover in Fp increases the density of a chemically homogeneous pyrolitic mantle by ~0.7%. It is a smooth and broad feature that should enhance convection in a chemically uniform mantle (22–24), especially in the spin crossover zone, which spans most of the lower mantle. This broad spin crossover also seems consistent with the lack of seismological evidence of a compositional transition and associated thermal boundary layers (39, 40) in the mid–lower mantle. In some slow regions beneath hot spots, similar reduction of *P* velocity heterogeneity at comparable depths is well documented

Table 1. Temperature gradients of bulk (K_S) and shear (G) moduli and density (ρ) of $Mg_{0.875}Fe_{0.125}O$ and $Mg_{0.79}Fe_{0.21}O$ at 75 GPa and several temperatures

		dK_S/dT, 10^{-3} GPa/K		dG/dT, 10^{-3} GPa/K		$d\rho/dT$, 10^{-3} gr/cm^3/K	
x	T (K)	HS/LS	MS	HS/LS	MS	HS/LS	MS
0.125	920	−12	−270	−11	−21	−0.08	−0.15
	1,400	−12	0	−11	−28	−0.08	−0.21
	1,850	−13	60	−11	−18	−0.09	−0.14
0.21	920	−12	−446	−10	−27	−0.08	−0.2
	1,400	−12	0	−11	−38	−0.09	−0.31
	1,850	−13	110	−11	−22	−0.09	−0.19

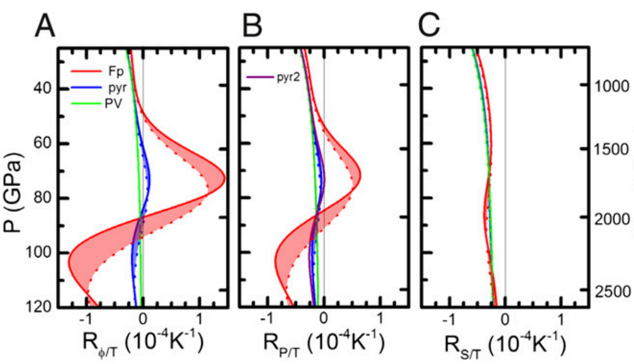

Fig. 2. Pressure dependence of thermally induced lateral variations in (*A*) bulk ($R_{\varphi/T} = \partial \ln V_\varphi/\partial T$), (*B*) longitudinal ($R_{P/T} = \partial \ln V_P/\partial T$), and (*C*) shear ($R_{S/T} = \partial \ln V_S/\partial T$) velocities in Fp, pyrolite (pyr), and perovskitic (PV) aggregates along adiabatic (26) (solid line) and superadiabatic (27) (dotted line) mantle geotherms. The pyrolite model contains 81 wt % of $(Mg_{0.92}Fe_{0.08})SiO_3$ (MgPv), 7 wt % $CaSiO_3$, and 12 wt % $Mg_{0.8125}Fe_{0.1875}O$ (Fp). The perovskitic aggregate contains 92 wt % of MgPv and 8 wt % $CaSiO_3$-Pv. $R_{P/T}$ = 0.0 at 73 GPa for an aggregate containing 75 wt % of MgPv, 18 wt % Fp, and 7 wt % $CaSiO_3$ (pyr2) along the adiabatic geotherm.

(41). For example, two low-velocity zones under the Hawaii hotspot are separated in the 1,500~2,000-km depth interval (41, 42). The large low-V_P structure extending from 2,000-km depth to the core mantle boundary northwest of Hawaii appears to be a tilted mantle plume feeding the Hawaiian hot spot. Present results suggest that both velocity structures could be part of a single continuous plume whose manifestation is suppressed between 1,500- and 2,000-km depth because of the spin crossover in Fp. Similar suppressions (41) or reductions (43) in lateral variations in V_P are also found under several other hot spots in similar depth intervals. The exact depth and magnitude of this effect should depend on temperatures and on lateral and radial variations in abundance and composition of Fp. However, it should be robust and an expected effect in a lower mantle containing nonnegligible amounts of Fp.

In contrast to $R^{pyr}_{\varphi/T}$ and $R^{pyr}_{P/T}$, $R^{pyr}_{S/T}$ remains negative and is only slightly affected by the spin crossover in Fp (Fig. 2*C*). Therefore, the spin crossover in Fp does not inhibit manifestation of lateral temperature variations in V_S. An analysis of velocity structures beneath more than 40 hot spots (44) indicated that far more continuous slow velocity structures extending all of the way from the core–mantle boundary to the surface could be identified in three *S* models than in two *P* tomography models, the Hawaii thermal structure being an example. This outcome seems broadly consistent with the suppressed expression of lateral temperature variations in *P* but not in *S* models expected because of a spin crossover in Fp.

The behavior of $R^{pyr}_{\varphi/T}$, $R^{pyr}_{P/T}$, and $R^{pyr}_{S/T}$ shown in Fig. 2 also implies that in a compositionally homogeneous lower mantle, anticorrelation between V_φ and V_S and decrease in correlation between V_P and V_S could be observed between ~1,500-km and ~2,000-km depth, where $R^{pyr}_{\varphi/T}$ is positive (Figs. 2*A* and 3 *A* and *B*). It has been shown that anticorrelation between V_φ and V_S in the D″ region (e.g., ref. 45), can be explained to a great extent by the postperovskite transition (46, 47). However, anticorrelation at shallower depths in the mantle is still debatable. Masters et al. (45) and Ishii and Tromp (48) observed very weak anticorrelation (or decorrelation) at mid–lower mantle depths. The recent joint geodynamic–tomographic model developed by Simmons et al. (49), however, shows anticorrelation below ~1,800-km depth. This was interpreted as a sign of coexisting thermal and compositional heterogeneities. The present study suggests a possible relationship between this anticorrelation and the spin crossover in Fp, although it does not exclude simultaneous compositional heterogeneity. The manifestation of the spin crossover in $R_{\varphi/S}$ or in $R_{P/S}$ depends on local temperatures and compositions (Fig. 3 and Fig. S4) but should be a robust phenomenon in a homogeneous pyrolitic mantle that could be misinterpreted as compositional heterogeneity.

A most striking sign of the spin crossover appears in the $R_{S/P}$ ($\partial \ln V_S/\partial \ln V_P$) heterogeneity ratio (Fig. 4). Along plausible mantle geotherms (26, 27) and for several homogeneous aggregates, $R_{S/P}$ is insensitive to composition outside the spin crossover zone, i.e., above 1,200-km depth (Fig. 4). This happens because mantle minerals produce similar $R_{S/P}$ values (50) in the absence of the spin crossover. In the spin crossover zone, $R_{S/P}$ is quite sensitive to the abundance and composition of Fp but remains relatively insensitive to the relative abundances of MgPv or CaPv. This behavior of $R_{S/P}$ with depth is remarkably similar to those seen in tomography models analyzed by Saltzer et al. (51). $R_{S/P}$ values in mantle regions away from subduction (nonslab regions) and beneath convergent margins (slab regions) are very similar above 1,200-km depths. Below 1,500-km depths, $R_{S/P}$ increases faster in nonslab regions. In the context of our results, this difference suggests smaller abundance of Fp and/or of iron in Fp in the slab region, which could be compatible in principle with a compositional heterogeneity related with the presence of mid-ocean ridge basalt (MORB) crust material (52) intermixed with pyrolite. In a homogeneous pyrolitic mantle, $R_{S/P}$ should be maximum between ~1,500-km and ~2,000-km depth where V_S and V_φ are most anticorrelated (Figs. 3*A* and 4).

Because the anomalous softening in V_P depends on the abundance and iron content of Fp, $R_{S/P}$ should be significantly affected by compositional heterogeneity altering these quantities. This effect is not considered here. Saltzer et al. (51) reported that $R_{S/P}$ reaches a maximum around 2,100 km in nonslab regions. However, in most seismic tomography models, values of $R_{S/P}$ increase with depth and do not show a peak within mid–lower mantle depths (45, 48). The present study suggests that the absence of a clear peak in $R_{S/P}$ or a peak above the 1,500–2,000-km depth interval could be used as an indirect argument in support of compositional heterogeneity, particularly a reduction in Fp abundance with depth (19). A peak at greater depths could be produced by a combination of factors, especially by a change in iron partitioning between MgPv and Fp throughout the spin crossover in Fp. This can increase its iron concentration and its spin crossover pressure (11).

The complex spin crossover in ferric iron in MgPv (28–31, 53) is too uncertain at the moment, and its effects are presently not

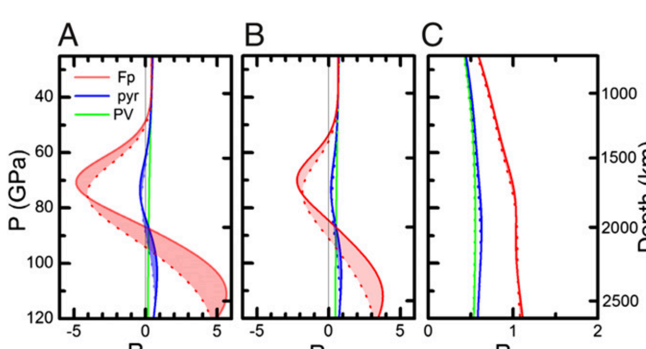

Fig. 3. Pressure dependence of thermally induced heterogeneity ratios (*A*) $R_{\varphi/S} = \partial \ln V_\varphi/\partial \ln V_S$, (*B*) $R_{P/S} = \partial \ln V_P/\partial \ln V_S$, and (*C*) $R_{\rho/S} = \partial \ln \rho/\partial \ln V_S$ in Fp, pyrolite, and perovskitic aggregates along adiabatic (26) (solid line) and superadiabatic (27) (dotted line) mantle geotherms. Aggregates are the same as in Fig. 2.

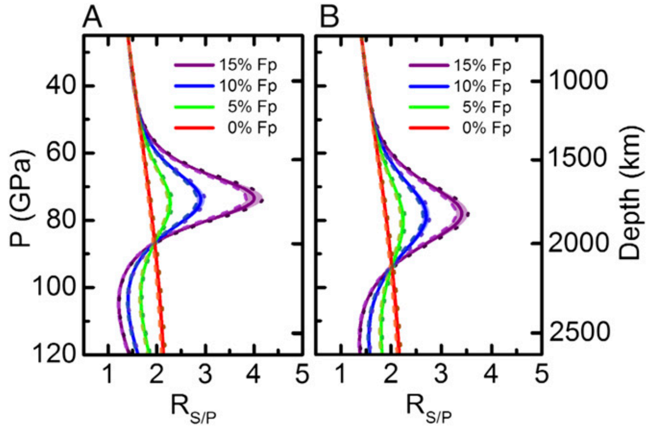

Fig. 4. Thermally induced $R_{S/P}(\partial \ln V_S/\partial \ln V_P)$ heterogeneity ratio in aggregates with various compositions along (*A*) adiabatic (26) and (*B*) superadiabatic (27) geotherms. Aggregates consist of $Mg_{0.8125}Fe_{0.1875}O$ in various amounts (see legend), $(Mg_{0.92}Fe_{0.08})SiO_3$, and CaPv in different proportions: 4 wt %, 7 wt %, and 10 wt % CaPv (dotted, solid, and short dashed lines, respectively).

understood, but it could also affect the $R_{S/P}$ profile in a compositionally homogeneous mantle. The recently discovered dissociation of iron-bearing MgPv into an iron-free MgPv and a hexagonal iron-rich phase (54) might also produce novel and unanticipated effects on lateral variations beyond 2,000-km depth. The mantle geotherm, which should depend on material properties that are strongly affected by the spin crossover (14), could also affect these $R_{S/P}$ profiles and shift the peak position (Fig. 4 *A* and *B*). Uncertainties in the calculated elastic anomalies in Fp at high temperatures cannot be ruled out either, because comparison with experiments has not been possible. The elasticities of CaPv and of other MORB phases at lower mantle conditions still need to be clarified to improve analyses of heterogeneities and/or radial velocity profiles in the deep lower mantle. However, the spin crossover in Fp is remarkably perceptible and its manifestation is exceptionally distinctive on lateral heterogeneities. In particular, a peak in $R_{S/P}$ near the mid–lower mantle could be viewed as a fingerprint of Fp presence in this region. Therefore, inclusion of Fp spin crossover effects in the analyses of tomography models should advance considerably our understanding of lower mantle structures.

Methods

The thermal elastic coefficients of Fp used in this work have recently been reported in detail by Wu et al. (ref. 20 and *Supporting Information*). They are based on a theoretical framework that was developed for spin crossover systems with low concentration of strongly correlated ions (up to $X_{Fe} \sim 0.2$) (9, 10, 14, 20). This formalism addresses Fp in the MS state as an ideal solid solution (ISS) of pure HS and LS states (9, 10, 14, 20). It is important to emphasize that this is a solid solution of two solid solutions, not of two (or three) end members, MgO and FeO (or MgO, $Fe^{HS}O$, and $Fe^{LS}O$). Extensive comparisons of equations of state and elastic moduli for different iron concentrations have been reported in figure 1 of ref. 20 and in *Supporting Information*. An important consequence of the formalism concerns the nature of the elastic anomalies. Elastic compliances, S^{ij}, are defined as

$$S^{ij} = \frac{1}{V}\frac{\partial^2 G}{\partial\sigma_i \partial\sigma_j}, \qquad [1]$$

where G is the Gibbs free energy of the solid solution, σ_i are the stress components in Voigt notation, and V is the volume. The elastic compliances of Fp in the MS then become (20)

$$S^{ij}V = nS^{ij}_{LS}V_{LS} + (1-n)S^{ij}_{HS}V_{HS} - \left(\frac{\partial G_{LS}}{\partial\sigma_j} - \frac{\partial G_{HS}}{\partial\sigma_j}\right)\frac{\partial n}{\partial\sigma_i}, \qquad [2]$$

where $n = n(P,T)$ is the fraction of LS states and G_{LS} and G_{HS} are Gibbs free energies of the pure LS and HS states, respectively. The last term in the right-hand side of Eq. **2** only appears in the MS state, where spin populations change with pressure or stress. This term causes elastic anomalies, as observed in the bulk modulus (10, 14, 20). In systems with cubic symmetry, anomalies in S^{11} and S^{12} should be present because $[\partial n/\partial\sigma_1]_{\sigma_1=0} \neq 0$. However, n is an even function of shear stress σ_4. Hence, $[\partial n/\partial\sigma_4]_{\sigma_4=0} = 0$, and no anomalies should occur in S^{44}. This indicates that observed anomalies in C_{44}, or $1/SS^{44}$ (15), virtually absent in measurements by Marquardt et al. (16), should be an extrinsic effect.

First-principles calculations of static of equations of state and elastic coefficients of HS and LS Fp were performed using a rotationally invariant version of the local density approximation plus Hubbard U potential (LDA+U) method (55) with U values as previously reported (9). Phonon spectra of MgO were calculated using density functional perturbation theory (56). Calculated force constants were then modified to reproduce the static elastic coefficients of Fp in pure HS and LS states. This is the vibrational virtual crystal model (14) that has been used in conjunction with the quasiharmonic approximation (57) to compute the thermal properties of Fp in HS, LS, and MS states and reproduce well the thermal elastic coefficients of Fp (20). Alternative vibrational density of states for Fp obtained with LDA+U also can be obtained (58). However, its predictive power remains questionable without inclusion of solid solution effects. Since the first calculation was performed (9), the LDA+U method has evolved. Today, U is calculated self-consistently (59), and the values of U_{sc} for iron in HS and LS states should be reinvestigated accordingly. As reported in ref. 20, we simply added a constant, E_{shift}, to the free energy curve of LS Fp to bring into agreement measured (16) and calculated anomalies. This simple energy shift raises the transition pressure from 33 to 45 GPa and does not change the absolute values of elastic coefficients or equations of state of HS and LS states. This energy shift also improves agreement between the midpoint of predicted and measured (13) high-temperature crossover pressure range.

The effect of the spin crossover in Fp on the elastic modulus of uniform aggregates with pyrolitic composition (1) was estimated along likely mantle geotherms (26, 27). Variations in mineral and aggregate compositions were investigated to estimate uncertainties in predicted effects of Fp on heterogeneities and their ratios (Figs. 1–4). The bulk and shear moduli of CaPv are those listed in Stixrude and Lithgow-Bertelloni's tables (60). The elastic moduli of MgPv are those reported earlier in ref. 61. The effect of iron on the elastic modulus of MgPv without the effect of its own spin crossover was included as reported in ref. 62. Finally, elastic coefficients of aggregates were computed using the Voigt-Reuss-Hill (63, 64) average. More details of the calculations are reported in *Supporting Information*.

ACKNOWLEDGMENTS. We thank R. O'Connell for bringing ref. 44 to our attention while this manuscript was under review and two referees for helpful comments. This work was supported by National Natural Science Foundation of China (41274087), State Key Development Program of Basic Research of China (2014CB845905), the Chinese Academy of Sciences International Partnership Program for Creative Research Teams, and National Science Foundation (EAR-1341862 and EAR-1047629).

1. Mcdonough WF, Sun SS (1995) The composition of the Earth. *Chem Geol* 120(3-4): 223–253.
2. Kesson SE, Fitz Gerald JD, Shelley JM (1998) Mineralogy and dynamics of a pyrolite lower mantle. *Nature* 39(6682):252–255.
3. Badro J, et al. (2003) Iron partitioning in Earth's mantle: Toward a deep lower mantle discontinuity. *Science* 300(5620):789–791.
4. Lin JF, et al. (2005) Spin transition of iron in magnesiowüstite in the Earth's lower mantle. *Nature* 436(7049):377–380.
5. Fei YW, et al. (2007) Spin transition and equations of state of (Mg, Fe)O solid solutions. *Geophys Res Lett* 34(17):L17307.
6. Mao Z, Lin JF, Liu J, Prakapenka VB (2011) Thermal equation of state of lower-mantle ferropericlase across the spin crossover. *Geophys Res Lett* 38(23):L23308.
7. Kantor I, et al. (2009) Short-range order and Fe clustering in Mg1-xFexO under high pressure. *Phys Rev B* 80(1):014204.
8. Lin JF, et al. (2007) Spin transition zone in Earth's lower mantle. *Science* 317(5845):1740–1743.
9. Tsuchiya T, Wentzcovitch RM, da Silva CRS, de Gironcoli S (2006) Spin transition in magnesiowüstite in earth's lower mantle. *Phys Rev Lett* 96(19):198501.
10. Wentzcovitch RM, et al. (2009) Anomalous compressibility of ferropericlase throughout the iron spin cross-over. *Proc Natl Acad Sci USA* 106(21):8447–8452.
11. Persson K, Bengtson A, Ceder G, Morgan D (2006) Ab initio study of the composition dependence of the pressure-induced spin transition in the $(Mg_{1-x},Fe_x)O$ system. *Geophys Res Lett* 33(16):L16306.
12. Zhuravlev KK, et al. (2010) Isothermal compression behavior of (Mg,Fe)O using neon as a pressure medium. *Phys Chem Miner* 37(7):465–474.

13. Komabayashi T, Hirose K, Nagaya Y, Sugimura E, Ohishi Y (2010) High-temperature compression of ferropericlase and the effect of temperature on iron spin transition. *Earth Planet Sci Lett* 297(3-4):691–699.
14. Wu Z, Justo JF, da Silva CRS, de Gironcoli S, Wentzcovitch RM (2009) Anomalous thermodynamic properties in ferropericlase throughout its spin crossover transition. *Phys Rev B* 80(1):014409.
15. Crowhurst JC, Brown JM, Goncharov AF, Jacobsen SD (2008) Elasticity of (Mg,Fe)O through the spin transition of iron in the lower mantle. *Science* 319(5862):451–453.
16. Marquardt H, et al. (2009) Elastic shear anisotropy of ferropericlase in Earth's lower mantle. *Science* 324(5924):224–226.
17. Marquardt H, Speziale S, Reichmann HJ, Frost DJ, Schilling FR (2009) Single-crystal elasticity of (Mg0.9Fe0.1)O to 81 GPa. *Earth Planet Sci Lett* 287(3-4):345–352.
18. Antonangeli D, et al. (2011) Spin crossover in ferropericlase at high pressure: A seismologically transparent transition? *Science* 331(6013):64–67.
19. Murakami M, Ohishi Y, Hirao N, Hirose K (2012) A perovskitic lower mantle inferred from high-pressure, high-temperature sound velocity data. *Nature* 485(7396):90–94.
20. Wu Z, Justo JF, Wentzcovitch RM (2013) Elastic anomalies in a spin-crossover system: Ferropericlase at lower mantle conditions. *Phys Rev Lett* 110(22):228501.
21. Cammarano F, Marquardt H, Speziale S, Tackley PJ (2010) Role of iron-spin transition in ferropericlase on seismic interpretation: A broad thermochemical transition in the mid mantle? *Geophys Res Lett* 37(3):L03308.
22. Bower DJ, Gurnis M, Jackson JM, Sturhahn W (2009) Enhanced convection and fast plumes in the lower mantle induced by the spin transition in ferropericlase. *Geophys Res Lett* 36(10):L10306.
23. Shahnas MH, Peltier WR, Wu Z, Wentzcovitch R (2011) The high-pressure electronic spin transition in iron: Potential impacts upon mantle mixing. *J Geophys Res* 116(B8): B08205.
24. Matyska C, Yuen DA, Wentzcovitch RM, Cizkova H (2011) The impact of variability in the rheological activation parameters on lower-mantle viscosity stratification and its dynamics. *Phys Earth Planet Inter* 188(1-2):1–8.
25. Saha S, Bengtson A, Crispin KL, Van Orman JA, Morgan D (2011) Effects of spin transition on diffusion of Fe2+ in ferropericlase in Earth's lower mantle. *Phys Rev B* 84(18):184102.
26. Brown JM, Shankland TJ (1981) Thermodynamic parameters in the Earth as determined from seismic profiles. *Geophys J R Astron Soc* 66(3):579–596.
27. Anderson OL (1982) The Earth's core and the phase-diagram of iron. *Philos Trans R Soc London A* 306(1492):21–35.
28. Hsu H, Blaha P, Cococcioni M, Wentzcovitch RM (2011) Spin-state crossover and hyperfine interactions of ferric iron in MgSiO(3) perovskite. *Phys Rev Lett* 106(11): 118501.
29. Catalli K, et al. (2010) Spin state of ferric iron in MgSiO3 perovskite and its effect on elastic properties. *Earth Planet Sci Lett* 289(1-2):68–75.
30. Potapkin V, et al. (2013) Effect of iron oxidation state on the electrical conductivity of the Earth's lower mantle. *Nat Commun* 4:1427.
31. Fujino K, et al. (2012) Spin transition of ferric iron in Al-bearing Mg-perovskite up to 200 GPa and its implication for the lower mantle. *Earth Planet Sci Lett* 317:407–412.
32. Murakami M, Hirose K, Kawamura K, Sata N, Ohishi Y (2004) Post-perovskite phase transition in MgSiO3. *Science* 304(5672):855–858.
33. Tsuchiya T, Tsuchiya J, Umemoto K, Wentzcovitch RA (2004) Phase transition in MgSiO3 perovskite in the earth's lower mantle. *Earth Planet Sci Lett* 224(3-4):241–248.
34. Oganov AR, Ono S (2004) Theoretical and experimental evidence for a post-perovskite phase of MgSiO3 in Earth's D″ layer. *Nature* 430(6998):445–448.
35. Irifune T, et al. (2010) Iron partitioning and density changes of pyrolite in Earth's lower mantle. *Science* 327(5962):193–195.
36. van der Hilst RD, Karason H (1999) Compositional heterogeneity in the bottom 1000 kilometers of Earth's mantle: Toward a hybrid convection model. *Science* 283(5409): 1885–1888.
37. Tackley PJ (2000) Mantle convection and plate tectonics: Toward an integrated physical and chemical theory. *Science* 288(5473):2002–2007.
38. Kellogg LH, Hager BH, van der Hilst RD (1999) Compositional stratification in the deep mantle. *Science* 283(5409):1881–1884.
39. Castle JC, van der Hilst RD (2003) Searching for seismic scattering off mantle interfaces between 800 km and 2000 km depth. *J Geophys Res* 108(B2):2095.
40. Vidale JE, Schubert G, Earle PS (2001) Unsuccessful initial search for a midmantle chemical boundary with seismic arrays. *Geophys Res Lett* 28(5):859–862.
41. Zhao DP (2007) Seismic images under 60 hotspots: Search for mantle plumes. *Gondwana Res* 12(4):335–355.
42. Ji Y, Nataf HC (1998) Detection of mantle plumes in the lower mantle by diffraction tomography: Theory. *Earth Planet Sci Lett* 159(3-4):87–98.
43. Nolet G, Karato SI, Montelli R (2006) Plume fluxes from seismic tomography. *Earth Planet Sci Lett* 248(3-4):685–699.
44. Boschi L, Becker TW, Steinberger B (2007) Mantle plumes: dynamic models and seismic images. *Geochem Geophys Geosystems* 8(10):Q10006.
45. Masters G, Laske G, Bolton H, Dziewonski AM (2000) The relative behavior of shear velocity, bulk sound speed, and compressional velocity in the mantle: Implications for chemical and thermal structure. *Earth's Deep Interior: Mineral Physics and Tomography From the Atomic to the Global Scale*, Geophysical Monograph Series, eds Karato S-I, Forte A, Liebermann R, Masters G, Stixrude L (Am Geophys Union, Washington, DC), Vol 117, pp 63–87.
46. Wentzcovitch RM, Tsuchiya T, Tsuchiya J (2006) MgSiO3 postperovskite at D″ conditions. *Proc Natl Acad Sci USA* 103(3):543–546.
47. Trampert J, Deschamps F, Resovsky J, Yuen D (2004) Probabilistic tomography maps chemical heterogeneities throughout the lower mantle. *Science* 306(5697):853–856.
48. Ishii M, Tromp J (2001) Even-degree lateral variations in the Earth's mantle constrained by free oscillations and the free-air gravity anomaly. *Geophys J Int* 145(1): 77–96.
49. Simmons NA, Forte AM, Boschi L, Grand SP (2010) GyPSuM: A joint tomographic model of mantle density and seismic wave speeds. *J Geophys Res* 115(B12):B12310.
50. Karato S, Karki BB (2001) Origin of lateral variation of seismic wave velocities and density in the deep mantle. *J Geophys Res* 106(B10):21771–21783.
51. Saltzer RL, van der Hilst RD, Karason H (2001) Comparing P and S wave heterogeneity in the mantle. *Geophys Res Lett* 28(7):1335–1338.
52. Hirose K, Fei YW, Ma YZ, Mao HK (1999) The fate of subducted basaltic crust in the Earth's lower mantle. *Nature* 397(6714):53–56.
53. Fujino K, et al. (2014) Spin transition and substitution of Fe 3+ in Al-bearing post-Mg-perovskite. *Phys Earth Planet Inter* 217:31–35.
54. Zhang L, et al. (2014) Disproportionation of (Mg,Fe)SiO_3 perovskite in Earth's deep lower mantle. *Science* 344(6186):877–882.
55. Cococcioni M, de Gironcoli S (2005) Linear response approach to the calculation of the effective interaction parameters in the LDA+U method. *Phys Rev B* 71(3):035105.
56. Baroni S, de Gironcoli S, Dal Corso A, Giannozzi P (2001) Phonons and related crystal properties from density-functional perturbation theory. *Rev Mod Phys* 73(2):515–562.
57. Wallace DC (1972) *Thermodynamics of Crystals* (Wiley, New York).
58. Fukui H, Tsuchiya T, Baron AQR (2012) Lattice dynamics calculations for ferropericlase with internally consistent LDA+U method. *J Geophys Res* 117(B12):B12202.
59. Kulik HJ, Cococcioni M, Scherlis DA, Marzari N (2006) Density functional theory in transition-metal chemistry: A self-consistent Hubbard U approach. *Phys Rev Lett* 97(10):103001.
60. Stixrude L, Lithgow-Bertelloni C (2005) Thermodynamics of mantle minerals—II. Phase equilibria. *Geophys J Int* 184(3):1180–1213.
61. Wentzcovitch RM, Karki BB, Cococcioni M, de Gironcoli S (2004) Thermoelastic properties of $MgSiO_{(3)}$-perovskite: Insights on the nature of the Earth's lower mantle. *Phys Rev Lett* 92(1):018501.
62. Kiefer B, Stixrude L, Wentzcovitch RM (2002) Elasticity of (Mg,Fe)SiO_3-Perovskite at high pressures. *Geophys Res Lett* 29(1):1539.
63. Watt JP, Davies GF, O'Connell RJ (1976) The elastic properties of composite materials. *Rev Geophys Space Phys* 50(4):6290–6295.
64. Watt JP (1979) Hashin–Shtrikman bounds on the effective elastic moduli of polycrystals with orthorhombic symmetry. *J Appl Phys* 50(10):6290–6295.
65. Dziewonski A, Andeson DL (1981) Preliminary reference Earth model. *Phys Earth Planet Inter* 25(4):297–356.

Supporting Information

Wu and Wentzcovitch 10.1073/pnas.1322427111

SI Methods

Ferropericlase (Fp) in the mixed spin (MS) state has been successfully described as an ideal solid solution (ISS) of pure high-spin (HS) and low-spin (LS) states (1–4). The Gibbs free energy of this MS state, $G(n,P,T)$, is

$$G(n,P,T) = nG_{LS}(P,T) + (1-n)G_{HS}(P,T) + G_{mix}, \qquad \textbf{[S1]}$$

where $n = n(P,T)$ is the fraction of LS states; G_{LS} and G_{HS} are Gibbs free energies of the pure LS and HS states, respectively; and G_{mix} is the free energy of mixing. This free energy formalism has provided a foundation for the theory developed to describe the elastic properties of Fp in the MS state, as reported in ref. 1. (See *Methods* for a brief summary.)

A combination of first-principles calculations and a model vibrational density of state (VDOS), the vibrational virtual crystal model (VVCM) (2, 3), were used to obtain G_{LS} and G_{HS} within the quasiharmonic approximation (5). The oxygen pseudopotential was generated by the Troullier–Martins method (6), in a $2s^2 2p^4$ configuration with local-p orbital and core radii $r(2s) = r(2p) = 1.45$ a.u. The magnesium pseudopotential was generated using the von Barth–Car method, with five different electronic configurations ($3s^2 3p^0$, $3s^1 3p^1$, $3s^1 3p^{0.5} 3d^{0.5}$, $3s^1 3p^{0.5}$, and $3s^1 3d^1$, with weights of 1.5, 0.6, 0.3, 0.3, 0.3, and 0.2, respectively) with local-d orbital, and core radii $r(3s) = r(3p) = r(3d) = 2.5$ a.u. The iron pseudopotential was generated using the modified Rappe–Rabe–Kaxiras–Joannopoulos method (7), in a $3d^7 4s^1$ configuration, with core radii of $r(4s) = (2.0, 2.2)$, $r(4p) = (2.2, 2.3)$, and $r(3d) = (1.6, 2.2)$ a.u., where the first value represents the norm-conserving core radius and the second one represents the ultrasoft radius. The electronic wave functions were expanded in a plane wave basis set, where a cutoff of 70 Ry provided converged results. The Brillouin zone was sampled by a $2 \times 2 \times 2$ k-point grid.

The calculations used a rotationally invariant version of the local density approximation adding a Hubbard potential (LDA+U), where U was computed by an internally consistent procedure (8). The values of U used here are the same as those used in ref. 4, where the dependences of U with supercell size, spin state, and pressure were carefully investigated. Atomic positions were always fully relaxed with forces determined by the LDA+U energy functional. Calculations were performed in a supercell with 64 atoms for the concentration $X_{Fe} = 0.1875$ (26 Mg, 32 O, and 6 Fe atoms), with substitutional ferrous iron in the magnesium site. Iron atoms were positioned in a way to maximize the interiron distances within the supercell. With such iron distribution, $X_{Fe} = 0.1875$ is the upper concentration limit in which iron–iron interactions are negligible in the calculation. Those interactions are expected to slightly increase the static transition pressure (9). This effect cannot be easily computed using the ideal solid solution formalism, given the strong dependence of those interactions on orbital ordering. To capture such phenomenology and reproduce the observed transition pressure at 300 K, the static enthalpy curves of HS Fp were shifted uniformly to increase the static transition pressure from 33 to 45 GPa, as recently reported in ref. 1. Such constant shift does not affect thermal equations of state or thermoelastic properties of Fp in HS or LS states.

The VDOSs of pure $Mg_{0.8125}Fe_{0.1875}O$ in HS and LS states, i.e., the VVCM (2, 3), were developed by modifying the largest interatomic force constants of MgO to reproduce the elastic constant of Fp in HS and LS states (2), which were calculated using LDA+U. The interatomic force constants of MgO were calculated using density functional perturbation theory (10). The VDOSs of HS and LS Fp were then obtained using these modified force constants, and the mass of Mg was replaced by the average mass of $Mg_{(0.9125)}Fe_{0.1875}$. This average mass mimics atomic disorder, an effect not included in other calculations of high-temperature Fp (11–13). Inclusion of the vibrational contribution to the free energy considerably improved agreement between experimental measurements (14–16) and our predicted pressure and temperature-dependent spin populations and compression curves at room temperature (2, 3).

A comparison between spin populations predicted by the VVCM and measurements is shown in Fig. S1. Some experimental data for $n = 0.5$ obtained by Lin et al. (14) on a sample with $X_{Fe} = 0.25$ and by Komabayashi et al. (15) on a sample with $X_{Fe} = 0.19$ are indicated by stars and squares, respectively. White and black lines correspond to $n = 0.5$ in our unshifted and shifted calculations, respectively. It can be seen that high-temperature measurements are still not in good agreement. At these iron concentrations, spin populations should not depend strongly on iron concentration. At low temperature the transition pressure for $X_{Fe} = 0.25$ and $X_{Fe} = 0.19$ are similar. However, there are large differences in the high-T behavior, which do not seem to be explained easily by the difference in iron concentration alone. As shown by others (see ref. 16 for a summary), the transition pressure increases with increasing iron concentration for $X_{Fe} \geq 0.25$. This trend is not reflected by these two sets of experimental data at high temperatures. It can also be seen that our (shifted) results on $X_{Fe} = 0.1875$ agree very well with data on a sample with $X_{Fe} = 0.19$ (15) and also with data by Lin et al. (14) at low temperatures.

Elastic Properties of the Pyrolitic Aggregate

The first step in the present work was to investigate the effect of the spin crossover in Fp on the elastic modulus of a uniform aggregate with pyrolitic composition (17) along a mantle geotherm (18). The considered aggregate consists of 12 wt % $Mg_{1-x}Fe_xO$ (Fp) with $X_{Fe} = 0.1875$ (Fp18.75), 81% $Mg_{1-y}Fe_ySiO_3$ with $y = 0.08$ (MgPv8), and 7% $CaSiO_3$ perovskite (CaPv). The bulk and shear modulus of CaPv are those listed in Stixrude and Lithgow-Bertelloni's tables (19). The first-principles elastic moduli of MgPv are those reported earlier by our group (20). The effect of iron on the elastic modulus of MgPv without the effect of its own spin crossover was included as reported in ref. 21. Theoretical investigations predict that HS ferrous iron does not undergo a spin state change to the LS state at lower mantle pressures (22). Instead, it displaces laterally with no significant density change (22). Spin crossover should happen only in ferric iron in the B site in MgPv (23, 24). Aluminum in MgPv displaces ferric iron from the B site and appears to prevent spin crossover in ferric iron (25, 26), but a consensus has not emerged on this issue yet (27, 28). However, the elastic modulus of MgPv is not noticeably affected by the spin crossover (29–31). Calculated elastic moduli, velocities, and density all agree well with values reported in the Preliminary Reference Earth Model (PREM) (32) along the lower mantle (Fig. S2). We previously reported a more enhanced bulk modulus softening in an aggregate of 20 wt % Fp18.75 and 80 wt % MgPv12. Results in the present aggregate produce elastic moduli and velocities more consistent with those reported in PREM (32) (Fig. S2). In this aggregate the maximum effect of the spin crossover happens at ~74 GPa.

Elastic Anomalies

The unusual effect of spin crossover on the elasticity of Fp is clearly reflected on the temperature dependence of all velocities. Both $\partial \ln V_\varphi / \partial \ln T$ ($R_{\varphi/T}$) and $\partial \ln V_S / \partial \ln T$ ($R_{S/T}$) are sensitive to temperature and pressure. However, their behaviors are quite different. In contrast to $R_{S/T}$, which is always negative, $R_{\varphi/T}$ can be positive throughout a large pressure range as shown in Fig. S3 *A* and *C*. The effect of the spin crossover is enormous. The maximum value of $R_{\varphi/T}$ at 1,000 K is 5×10^{-4}/K, which is about 60 times the maximum $|R_{\varphi/T}|$ of a Pv aggregate (Fig. S3*G*) at the same pressure. Even at 3,000 K, the maximum value, 8×10^{-5}/K, is still about 13 times that of the $|R_{\varphi/T}|$ in a Pv aggregate (Fig. S3*G*) at the same pressure. Therefore, although the lower mantle should have less than 20 wt % of Fp, we may still expect positive $R_{\varphi/T}$ in some pressure range, even at 3,000 K (Fig. S3*D*). However, $R_{S/T}$ is always negative in a pyrolitic aggregate (Fig. S3*F*). The pressure and temperature dependence of $\partial \ln V_P / \partial \ln T$ ($R_{P/T}$) is similar to that of $R_{\varphi/T}$ but with smaller variations (Fig. S3 *A* and *B*). $R_{P/T}$ of a pyrolitic aggregate (Fig. S3*E*) can be positive in some pressure range only at relatively low temperatures (less than 2,000 K). Without spin crossover, $R_{\varphi/S}$ of Fp is always positive with a value similar to those of other silicate minerals such as MgPv in Fig S3*E*. In the presence of the spin crossover, $R_{\varphi/S}$ can be negative with a minimum reaching −12.8 (−3.2) at 1,000 K (3,000 K). $R_{\varphi/S}$ of Fp and of pyrolite shown in Fig. S4 *A* and *C* are negative in the same pressure region where their $R_{\varphi/T}$ is positive. Namely, V_φ and V_S can be negatively correlated in a compositionally homogeneous pyrolitic lower mantle. Another striking feature of the spin crossover is that it can lead to an unusually large positive $R_{\varphi/S}$ ($R_{P/S}$); for example, the maximum of $R_{\varphi/S}$ ($R_{P/S}$) of Fp at 2,000 K is about 6.3 (4.4) at ~100 GPa (Figs. S3*B* and S4*A*). Changes in V_S or ρ caused by the spin crossover are similar in nature. $\partial \ln \rho / \partial \ln T$ ($R_{\rho/T}$) is also negative, and V_S and ρ are positively correlated.

1. Wu Z, Justo JF, Wentzcovitch RM (2013) Elastic anomalies in a spin-crossover system: Ferropericlase at lower mantle conditions. *Phys Rev Lett* 110(22):228501.
2. Wu Z, Justo JF, da Silva CRS, de Gironcoli S, Wentzcovitch RM (2009) Anomalous thermodynamics properties in ferropericlase throughout its spin crossover transition. *Phys Rev B* 80(1):014409.
3. Wentzcovitch RM, et al. (2009) Anomalous compressibility of ferropericlase throughout the iron spin cross-over. *Proc Natl Acad Sci USA* 106(21):8447–8452.
4. Tsuchiya T, Wentzcovitch RM, da Silva CRS, de Gironcoli S (2006) Spin transition in magnesiowüstite in earth's lower mantle. *Phys Rev Lett* 96(19):198501.
5. Wallace DC (1972) *Thermodynamics of Crystals* (Wiley, New York).
6. Troullier N, Martins JL (1991) Efficient pseudopotentials for plane-wave calculations. *Phys Rev B Condens Matter* 43(3):1993–2006.
7. Rappe AM, Rabe KM, Kaxiras E, Joannopoulos JD (1990) Optimized pseudopotentials. *Phys Rev B Condens Matter* 41(2):1227–1230.
8. Cococcioni M, de Gironcoli S (2005) Linear response approach to the calculation of the effective interaction parameters in the LDA+U method. *Phys Rev B* 71(3):035105.
9. Persson K, Bengtson A, Ceder G, Morgan D (2006) Ab initio study of the composition dependence of the pressure-induced spin transition in the (Mg1-x,Fe-x)O system. *Geophys Res Lett* 33(16):L16306.
10. Baroni S, de Gironcoli S, Dal Corso A, Giannozzi P (2001) Phonons and related crystal properties from density-functional perturbation theory. *Rev Mod Phys* 73(2):515–562.
11. Fukui H, Tsuchiya T, Baron AQR (2012) Lattice dynamics calculations for ferropericlase with internally consistent LDA+U method. *Geophys Res* 117(B12):B12202.
12. Scanavino I, Belousov R, Prencipe M (2012) Ab initio quantum-mechanical study of the effects of the inclusion of iron on thermoelastic and thermodynamic properties of periclase (MgO). *Phys Chem Miner* 39(8):649–663.
13. Scanavino I, Prencipe M (2013) Ab-initio determination of high-pressure and high-temperature thermoelastic and thermodynamic properties of low-spin (Mg1-xFex)O ferropericlase with x in the range. *Am Mineral* 98(7):1270–1278.
14. Lin JF, et al. (2007) Spin transition zone in Earth's lower mantle. *Science* 317(5845): 1740–1743.
15. Komabayashi T, Hirose K, Nagaya Y, Sugimura E, Ohishi Y (2010) High temperature compression of ferropericlase and the effect of temperature on the iron spin transition. *Earth Planet Sci Lett* 297(3-4):691–699.
16. Fei YW, et al. (2007) Spin transition and equations of state of (Mg, Fe)O solid solutions. *Geophys Res Lett* 34(17):L17307.
17. Mcdonough WF, Sun SS (1995) The composition of the Earth. *Chem Geol* 120(3-4): 223–253.
18. Boehler R (2000) High-pressure experiments and the phase diagram of lower mantle and core materials. *Rev Geophys* 38(2):221–245.
19. Stixrude L, Lithgow-Bertelloni C (2005) Thermodynamics of mantle minerals—II. phase equilibria. *Geophys J Int* 184(3):1180–1213.
20. Wentzcovitch RM, Karki BB, Cococcioni M, de Gironcoli S (2004) Thermoelastic properties of $MgSiO_{(3)}$-perovskite: Insights on the nature of the Earth's lower mantle. *Phys Rev Lett* 92(1):018501.
21. Kiefer B, Stixrude L, Wentzcovitch RM (2002) Elasticity of (Mg,Fe)SiO3-perovskite at high pressures. *Geophys Res Lett* 29(1):1539.
22. Hsu H, Umemoto K, Blaha P, Wentzcovitch RM (2010) Spin states and hyperfine interactions of iron in $(Mg,Fe)SiO_3$ perovskite under pressure. *Earth Planet Sci Lett* 294(1-2):19–26.
23. Hsu H, Blaha P, Cococcioni M, Wentzcovitch RM (2011) Spin-state crossover and hyperfine interactions of ferric iron in MgSiO(3) perovskite. *Phys Rev Lett* 106(11): 118501.
24. Wentzcovitch RM, Hsu H, Umemoto K (2012) First-principles studies of spin-state crossovers of iron in perovskite. *Eur J Mineral* 24(5):851–862.
25. Potapkin V, et al. (2013) Effect of iron oxidation state on the electrical conductivity of the Earth's lower mantle. *Nat Commun* 4:1427.
26. Hsu H, Yu YGG, Wentzcovitch RM (2012) Spin crossover of iron in aluminous MgSiO3 perovskite and post-perovskite. *Earth Planet Sci Lett* 359:34–39.
27. Catalli K, et al. (2010) Spin state of ferric iron in $MgSiO_3$ perovskite and its effect on elastic properties. *Earth Planet Sci Lett* 289(1-2):68–75.
28. Lin JF, Speziale S, Mao Z, Marquardt H (2013) Effects of the electronic spin transitions of iron in lower mantle minerals: Implications for deep mantle geophysics and geochemistry. *Rev Geophys* 51(2):244–275.
29. Lin JF, et al. (2012) Electronic spin states of ferric and ferrous iron in the lower-mantle silicate perovskite. *Am Mineral* 97(4):592–597.
30. Lundin S, et al. (2008) Effect of Fe on the equation of state of mantle silicate perovskite over 1 Mbar. *Phys Earth Planet Inter* 168(1-2):97–102.
31. Fujino K, et al. (2012) Spin transition of ferric iron in Al-bearing Mg-perovskite up to 200 GPa and its implication for the lower mantle. *Earth Planet Sci Lett* 317:407–412.
32. Dziewonski AM, Anderson DL (1981) Preliminary Reference Earth Model. *Phys Earth Planet Inter* 25(4):297–356.

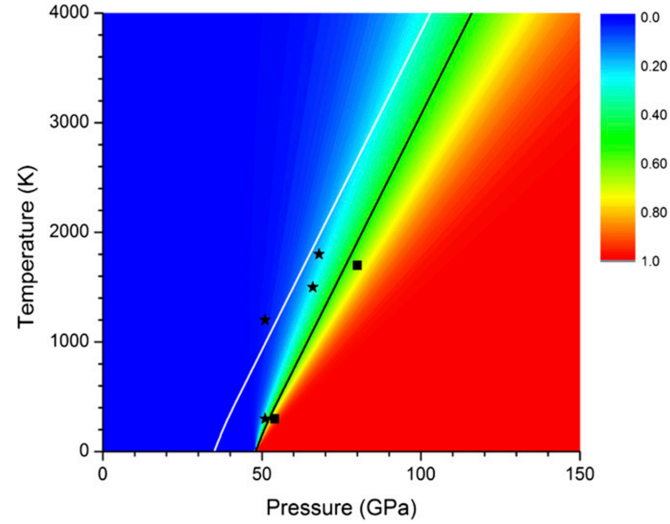

Fig. S1. Predicted fraction of low spin iron, $n(P,T)$, for $X_{Fe} = 0.1875$. Black and white lines correspond to the midpoint of the crossover, i.e., $n = 0.5$, with and without energy shift, respectively. Stars represent $n = 0.5$ in data by Lin et al. (14) for Fp with $X_{Fe} = 0.25$. Solid squares represent $n = 0.5$ in data by Komabayashi et al. (15) for Fp with $X_{Fe} = 0.19$.

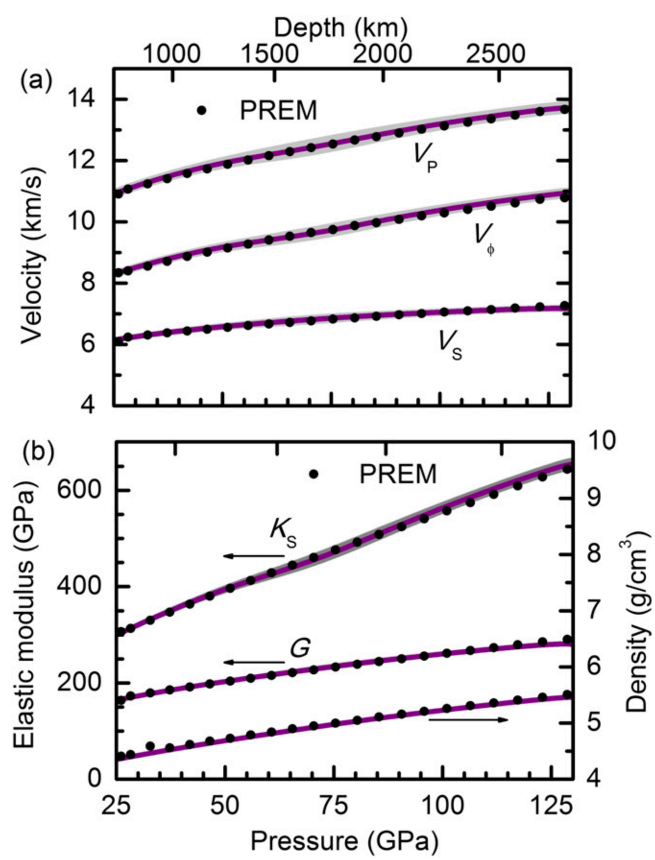

Fig. S2. (*A*) Velocities and (*B*) elastic moduli and density of a uniform pyrolitic aggregate with 81 wt % of MgPv8, 12 wt % Fp18.75, and 7% CaPv along the Boehler mantle geotherm (18) compared with PREM (32).

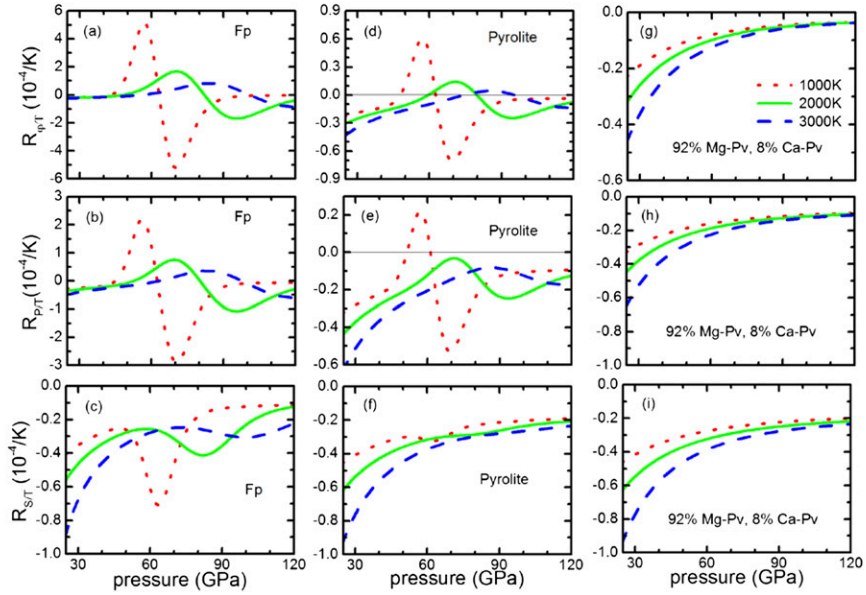

Fig. S3. Pressure dependence of lateral heterogeneity in bulk ($R_{\varphi/T} = \partial \ln V_\varphi/\partial T$), longitudinal ($R_{P/T} = \partial \ln V_P/\partial T$), and shear ($R_{S/T} = \partial \ln V_S/\partial T$) velocities at 1,000 K, 2,000 K, and 3,000 K. (*A–C*) An aggregate of Fp18.75; (*D–F*) a pyrolithic aggregate with 81 wt % of MgPv8, 12 wt % Fp18.75, and 7 wt % CaPv; and (*G–I*) a perovskitic aggregate with 92 wt % MgPv8 and 8 wt % CaPv.

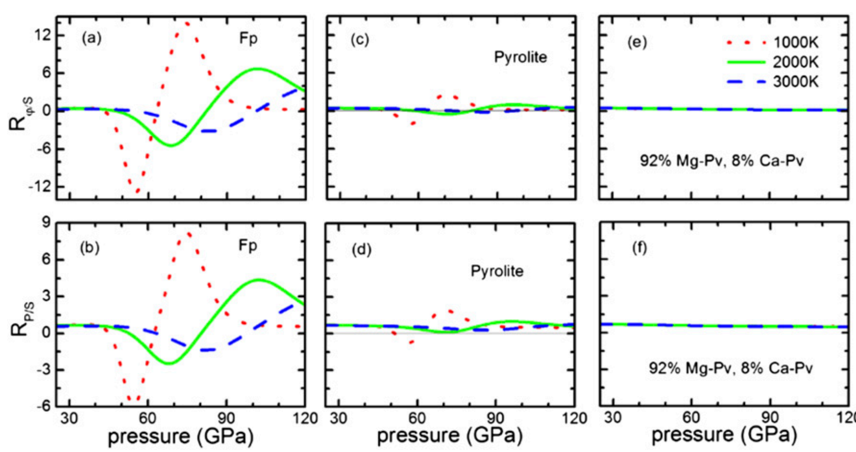

Fig. S4. Pressure dependence of thermally induced heterogeneity ratios $R_{\varphi/S} = \partial \ln V_\varphi/\partial \ln V_S$ and $R_{P/S} = \partial \ln V_P/\partial \ln V_S$ at 1,000 K, 2,000 K, and 3,000 K. (*A* and *B*) An aggregate of Fp18.75; (*C* and *D*) a pyrolithic aggregate containing 81 wt % of MgPv8, 12 wt % Fp18.75, and 7% CaPv; and (*E* and *F*) a perovskitic aggregate containing 92 wt % MgPv8 and 8% CaPv.f.